Journal of Marine Science and Application (2026) 25: 82-94
https://doi.org/10.1007/s11804-025-00693-6

RESEARCH ARTICLE

Load of the Small-Scale Vertical Cylinder in a Wave–Current Field

Mingjie Li[1], Binbin Zhao[1] and Wengyang Duan[1]

Received: 11 November 2024 / Accepted: 03 March 2025

Abstract

Studies of wave–current interactions are vital for the safe design of structures. Regular waves in the presence of uniform, linear shear, and quadratic shear currents are explored by the High-Level Green–Naghdi model in this paper. The five-point central difference method is used for spatial discretization, and the fourth-order Adams predictor–corrector scheme is employed for marching in time. The domain-decomposition method is applied for the wave–current generation and absorption. The effects of currents on the wave profile and velocity field are examined under two conditions: the same velocity of currents at the still-water level and the constant flow volume of currents. Wave profiles and velocity fields demonstrate substantial differences in three types of currents owing to the diverse vertical distribution of current velocity and vorticity. Then, loads on small-scale vertical cylinders subjected to regular waves and three types of background currents with the same flow volume are investigated. The maximum load intensity and load fluctuation amplitude in uniform, linear shear, and quadratic shear currents increase sequentially. The stretched superposition method overestimates the maximum load intensity and load fluctuation amplitude in opposing currents and underestimates these values in following currents. The stretched superposition method obtains a poor approximation for strong nonlinear waves, particularly in the case of the opposing quadratic shear current.

Keywords Wave-current interaction; Cylinder load; HLGN model; Morison equation; Regular waves

1 Introduction

Waves and currents coexist extensively in oceanic environments. The wave–current interaction has remarkable influences on the hydrodynamics of the fluid and the loading on marine structures, such as floating offshore wind turbines, offshore platforms, sea-crossing bridges, and aquaculture cages. Thus, investigating the wave–current interaction holds immense importance for the safe design of structures.

Laboratory experiments are an important approach to examine the interactions between waves and background currents. Thomas (1990) performed experiments on regular waves in following shear currents. The results revealed the importance of the vorticity in wave–current interactions. Swan (1990) studied regular waves in the presence of linear shear currents. Later, Swan et al. (2001) extended laboratory experiments to waves spreading in nonlinear shear currents. Umeyama (2011) presented experimental data on the particle velocities and trajectories of waves in the following uniform currents using coupled particle image velocimetry (PIV) and particle tracking velocimetry (PTV) measurements. The linear superposition of waves and currents cannot accurately explain the horizontal velocity. Subsequently, Umeyama (2017) gauged the dynamic pressure of regular waves in the presence of uniform currents. Chen et al. (2017) presented experimental wave profile data in the presence of uniform currents. The numerical wave-profile results of the higher-order boundary element method were consistent with the experimental data. Steer et al. (2020) experimentally investigated the dispersion and stability of weakly nonlinear waves in opposing linear shear currents. The results showed that opposing linear shear currents increase wavelength and improve stability compared with uniform currents with the same surface velocity.

Numerous studies examined the linear or weakly nonlinear steady solutions of wave–current interactions. Thomas (1981) obtained linear solutions for regular waves in arbi-

Article Highlights

- Regular waves in the presence of uniform, linear shear, and quadratic shear currents are investigated by employing the High-Level Green–Naghdi model.
- The wave profile and velocity field of regular waves are studied separately for three types of currents with the same velocity at the still-water level and three types of currents with constant flow volume.
- Loads of the small-scale vertical cylinder in wave–current fields are investigated under the same flow volume for the three types of currents.

✉ Binbin Zhao
zhaobinbin@hrbeu.edu.cn

[1] College of Shipbuilding Engineering, Harbin Engineering University, Harbin 150001, China

trary currents. Kirby and Chen (1989) developed a perturbation method for linear waves in the presence of weak currents. Banihashemi et al. (2017) followed Kirby and Chen (1989) and approximated the wave action flux velocity in strongly sheared currents. Baddour and Song (1998) derived the second-order solutions of waves in shear currents and the expressions for the stream function and dispersion relation. Swan and James (2000) established a perturbation method to derive the second solution for small amplitude waves in arbitrary currents. Hsu et al. (2009) acquired a third-order solution for the particle trajectory of regular waves in uniform currents in the Lagrangian form. Constantin et al. (2015) discussed the second- and third-order approximations of the wave profile, velocity field, and pressure for waves in the presence of linear shear currents. Touboul et al. (2016) extended the mild-slope equation to study linear waves in the presence of background currents. Li and Ellingsen (2019) obtained a direct integration method to study linear waves in the presence of arbitrary currents.

Fully nonlinear steady solutions of wave–current interactions are more complex to investigate. Dalrymple (1974) established a numerical perturbation procedure to explain regular waves in linear shear currents using the series expansion of the stream function formulation. Dalrymple and Cox (1976) examined regular waves in the presence of trigonometric and hyperbolic currents by extending the method of Dalrymple (1974). Constantin and Strauss (2004) verified the existence of large amplitude waves in arbitrary currents. Ko and Strauss (2008) investigated waves in currents with shear at the top, middle, or bottom. Choi (2009) developed a closed system of exact elevation equations to examine waves in linear shear currents. The results revealed that the maximum wave amplitude with following currents is much smaller than that without currents. Chen and Basu (2021) applied a numerical continuation method based on a fixed mean water depth formulation to investigate waves in arbitrary currents.

Lately, the time-domain simulation has been generally used to analyze regular waves in the presence of background currents. Nwogu (2009) employed a boundary integral method to study waves in background currents. Zhang et al. (2014) used a Reynolds-Averaged Navier–Stokes solver to simulate waves in uniform currents. The results presented that interactions of shorter period waves and currents lead to a larger diminution in the wave height and velocity magnitude around the water surface. Son and Lynett (2014) offered a set of depth-integrated equations to depict waves in arbitrary currents. Duan et al. (2016) examined the influences of uneven bottoms on waves in the presence of uniform currents by using the High-Level Green–Naghdi (HLGN) model. Abbasnia and Guedes Soares (2018) developed the Mixed Eulerian–Lagrangian scheme to simulate waves in uniform currents. Chen and Zou (2019) employed OpenFOAM to examine shallow water waves in the presence of uniform and linear shear currents. The effects of currents on near resonant triad wave interactions were investigated. Yang and Liu (2022) developed the depth-integrated wave–current model based on the work of Yang and Liu (2020) to simulate waves in background currents. Kumar and Hayatdavoodi (2023a, 2023b) analyzed the effects of currents on deep and shallow water waves, including changes in wave height, wavelength, particle velocity, and the pressure field. Zhao et al. (2023) built an effective method for wave–current generation and absorption based on the HLGN model to simulate regular waves in uniform, linear shear, and nonlinear shear currents.

Earlier studies investigated the effects of uniform and linear shear currents on the flow field of regular waves (Swan, 1990; Chen and Zou, 2019; Chen and Basu, 2021; Kumar and Hayatdavoodi, 2023b; Steer et al., 2020). However, few studies compared the effects of uniform, linear shear, and quadratic shear currents on the flow field of regular waves. Loads of the small-scale vertical cylinder in regular waves under the three types of currents are required to be further examined. Hence, this work aims to 1) investigate the effects of uniform, linear shear, and quadratic shear currents on wave profiles and velocity fields of regular waves and 2) examine the loads of the small-scale vertical cylinder in regular waves under the three types of currents with the same flow volume. The HLGN model is used to investigate these problems. This paper is organized as follows. The HLGN model is presented in Section 2. The numerical results are explained in Section 3. Conclusions are derived in Section 4.

2 HLGN model

In this paper, the 2D regular wave in the presence of ambient currents is considered. The fluid is assumed to be incompressible and inviscid. In the HLGN model, the origin of the 2D Cartesian coordinate system is at the still-water level (SWL), x (positive to the right) is the horizontal axis, and z (positive up) is the vertical axis. $z = \eta(x, t)$ denotes the free surface, $z = -h$ signifies the bottom, h represents the constant water depth, and t is the time.

The continuity equation is stated as follows:

$$\frac{\partial u}{\partial x} + \frac{\partial w}{\partial z} = 0 \tag{1}$$

where u and w are the horizontal and vertical velocity components, respectively.

The Euler equations are expressed as follows:

$$\frac{\partial u}{\partial t} + u\frac{\partial u}{\partial x} + w\frac{\partial u}{\partial z} = -\frac{1}{\rho}\frac{\partial p}{\partial x} \tag{2}$$

$$\frac{\partial w}{\partial t} + u\frac{\partial w}{\partial x} + w\frac{\partial w}{\partial z} = -\frac{1}{\rho}\left(\frac{\partial p}{\partial z} + \rho g\right) \tag{3}$$

where ρ represents the constant fluid-mass density, p denotes the pressure, and g signifies the gravitational acceleration, which is 9.81 m/s^2 in this paper.

The kinematic boundary conditions are stated as follows:

$$w - \frac{\partial \eta}{\partial t} - u\frac{\partial \eta}{\partial x} = 0,\ \ z = \eta(x,t) \tag{4}$$

$$w = 0,\ \ z = -h \tag{5}$$

The dynamic boundary condition is expressed as follows:

$$p = 0,\ \ z = \eta(x,t) \tag{6}$$

In this paper, the velocity field follows a polynomial shape.

$$u(x,z,t) = u_c(z) + u^*(x,z,t) = \sum_{n=0}^{K-1} u_{cn} z^n + \sum_{n=0}^{K-1} u_n^*(x,t) z^n \tag{7}$$

$$w(x,z,t) = \sum_{n=0}^{K} w_n^*(x,t) z^n \tag{8}$$

where u_c denotes the background current velocity; u^* represents the horizontal wave-induced velocity; u_{cn} signifies the background current velocity coefficients, u_n^* and w_n^* are the unknown horizontal and vertical wave-induced velocity coefficients to be solved, respectively; K is the level of the HLGN model. u_{cn} and u_n^* satisfy the following:

$$u_c(z) = \sum_{n=0}^{K-1} u_{cn} z^n \tag{9}$$

$$u^*(x,z,t) = \sum_{n=0}^{K-1} u_n^*(x,t) z^n \tag{10}$$

Eqs. (7) and (8) are substituted into Eq. (1), and the following expression is derived:

$$w_n^* = -\frac{1}{n}\frac{\partial u_{n-1}^*}{\partial x},\ \ n = 1, 2, \cdots, K \tag{11}$$

Eqs. (7) and (8) are substituted into Eqs. (4) and (5), and the following expression is derived:

$$\frac{\partial \eta}{\partial t} = \sum_{n=0}^{K} \eta^n \left(w_n^* - u_{cn}\frac{\partial \eta}{\partial x} - u_n^*\frac{\partial \eta}{\partial x}\right) \tag{12}$$

$$w_0^* = -\sum_{n=1}^{K} w_n^* (-h)^n \tag{13}$$

Eqs. (11) and (13) are used to establish the relationship between u_n^* and w_n^*, and to eliminate the vertical wave-induced velocity coefficient w_n^*.

Eqs. (7) and (8) are substituted into Eqs. (2) and (3), each is multiplied term by z^n, integration is performed from $-h$ to η along the vertical direction, Eq. (6) is considered, the term about p is eliminated, and the following equation is obtained:

$$\frac{\partial}{\partial x}\left(G_n + gS1_n\right) + nE_{n-1} - (-h)^n \frac{\partial}{\partial x}\left(G_0 + gS1_0\right) = 0,\quad n = 1, 2, \cdots, K \tag{14}$$

where

$$E_n = \sum_{m=0}^{K}\left(\frac{\partial u_m^*}{\partial t} S2_{mn} + \frac{\partial u_m^*}{\partial x} Q_{mn} + u_{cm} H_{mn} + u_m^* H_{mn}\right) \tag{15}$$

$$G_n = \sum_{m=0}^{K}\left(\frac{\partial w_m^*}{\partial t} S2_{mn} + \frac{\partial w_m^*}{\partial x} Q_{mn} + w_m^* H_{mn}\right) \tag{16}$$

$$S1_n = \int_{-h}^{\eta} z^n \mathrm{d}z,\ \ S2_{mn} = \int_{-h}^{\eta} z^{m+n}\mathrm{d}z,\quad S3_{mrn} = \int_{-h}^{\eta} z^{m+r+n}\mathrm{d}z,\ \ S4_{mrn} = m\int_{-h}^{\eta} z^{m+r+n-1}\mathrm{d}z \tag{17}$$

$$Q_{mn} = \sum_{r=0}^{K}\left(u_{cr} S3_{mrn} + u_r^* S3_{mrn}\right),\ \ H_{mn} = \sum_{r=0}^{K} w_r^* S4_{mrn} \tag{18}$$

$$u_{cK} = 0,\ \ u_K^* = 0 \tag{19}$$

The number of unknowns is $K + 1$, which are η and $u_n^*(n = 0, 1, \cdots, K-1)$. $K + 1$ equations are supplied by Eqs. (12) and (14). This system of equations is closed and solvable.

To solve the HLGN model, Eq. (14) is restated as follows:

$$\tilde{\boldsymbol{A}}\dot{\boldsymbol{\xi}}_{,xx} + \tilde{\boldsymbol{B}}\dot{\boldsymbol{\xi}}_{,x} + \tilde{\boldsymbol{C}}\dot{\boldsymbol{\xi}} = \boldsymbol{f} \tag{20}$$

where $\boldsymbol{\xi} = \left[u_0^*, u_1^*, \cdots, u_{K-1}^*\right]^{\mathrm{T}}$. The dot over $\boldsymbol{\xi}$ is the time derivative, and the subscript comma represents the differentiation with respect to the indicated variable. $\tilde{\boldsymbol{A}}$, $\tilde{\boldsymbol{B}}$, $\tilde{\boldsymbol{C}}$, and $\boldsymbol{f}$ are functions of η, $\boldsymbol{\xi}$, and their spatial derivatives. The spatial derivative is acquired by using the five-point central difference method, and the fourth-order Adams predictor–corrector scheme is employed for time stepping. The algorithm is discussed in detail by Zhao et al. (2014). The domain-decomposition method is used for the wave–current generation and absorption, as presented in Figure 1. The computational domain is divided into five parts: linear, transition, nonlinear, transition, and linear regions. In the linear regions ($0 \leqslant x \leqslant x_1$ and $x_4 \leqslant x \leqslant x_5$), the linear equations are solved. A fully nonlinear equation system is applied in the nonlinear region ($x_2 \leqslant x \leqslant x_3$). The two sys-

tems are matched by the transition regions. The results of the HLGN model are acquired from the waves in the nonlinear region. The domain-decomposition method and the validation results are presented by Zhao et al. (2023).

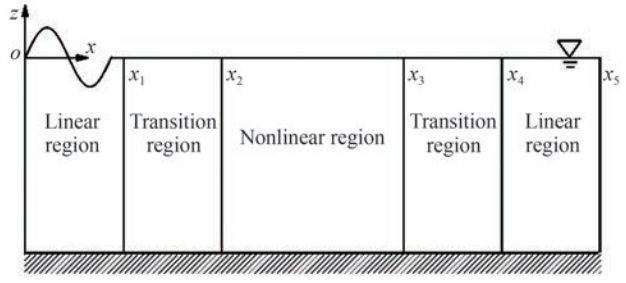

Figure 1 Sketch of the computational domain

3 Results and discussion

The HLGN model is employed to simulate regular waves in the presence of uniform, linear shear, and quadratic shear currents. The effects of currents on the wave profile and velocity field of regular waves are studied under two conditions: same velocity of currents at the SWL and constant flow volume of currents. Then, the loads of the small-scale vertical cylinder in regular waves under the three types of currents with the same flow volume are examined.

3.1 Currents with the same velocity at the SWL

In this section, the regular waves in the presence of background currents with the same velocity at the SWL are analyzed by using the HLGN model.

3.1.1 Numerical cases

The background currents are depicted as $u_c = U(1 + z/h)^n$ ($n = 0, 1, 2$), where U is the current velocity at the SWL. When $n = 0$, 1, and 2, the background currents correspond to uniform, linear shear, and quadratic shear currents, respectively. The parameters of the cases are listed in Table 1, where H is the wave height, T is the wave period, and $c_0 = \sqrt{gh}$. In two cases, the water depth is $h = 2.0$ m, the wave height is $H = 0.075$ m, and the wave period is $T = 1.325$ s. The steepness and dispersion of regular waves without currents are $H/\lambda_0 = 0.027\,4$ and $h/\lambda_0 = 0.730$, respectively, where λ_0 is the linear wavelength without currents. The computational domain is18λ long (λ represents the linear wavelength in the presence of currents). The lengths of the linear, transition, and nonlinear regions are λ, 4λ, and 8λ, respectively.

The current velocity profiles for uniform, linear shear, and quadratic shear currents are presented in Figure 2. The velocity of the uniform current is constant in the vertical direction, whereas the velocities of the linear shear and quadratic shear currents are strongest at the SWL and decrease

Table 1 Parameters of regular waves in background currents with the same velocity at the SWL

Case	h (m)	H (m)	T (s)	U/c_0	Current type
1	2.0	0.075	1.325	−0.034	Uniform
2	2.0	0.075	1.325	−0.034	Linear shear
3	2.0	0.075	1.325	−0.034	Quadratic shear
4	2.0	0.075	1.325	0.034	Uniform
5	2.0	0.075	1.325	0.034	Linear shear
6	2.0	0.075	1.325	0.034	Quadratic shear

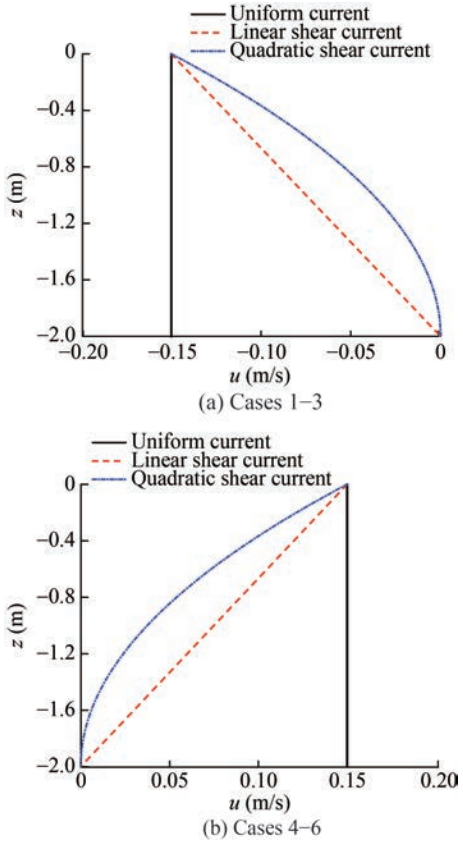

Figure 2 Current velocity profile of three types of background currents, Cases 1–6

along the water depth. At the free surface, the velocities of the three types of background currents are the same. At the bottom, the velocities of the shear currents are zero, whereas the strength of the uniform current is considerably greater than that of the shear currents. Excluding the SWL and bottom, the uniform current is the strongest, and the quadratic shear current is the weakest. Hence, the depth-averaged velocity of the uniform current is the highest and indicates that the flow volume is the largest, whereas the depth-averaged velocity of the quadratic current is the lowest and signifies that the flow volume is the least.

3.1.2 Wave profile

In this subsection, the wave profile of regular waves is presented. Regular waves in the presence of quadratic shear

currents are shown as an example, and the wave profiles at different times are demonstrated in Figure 3.

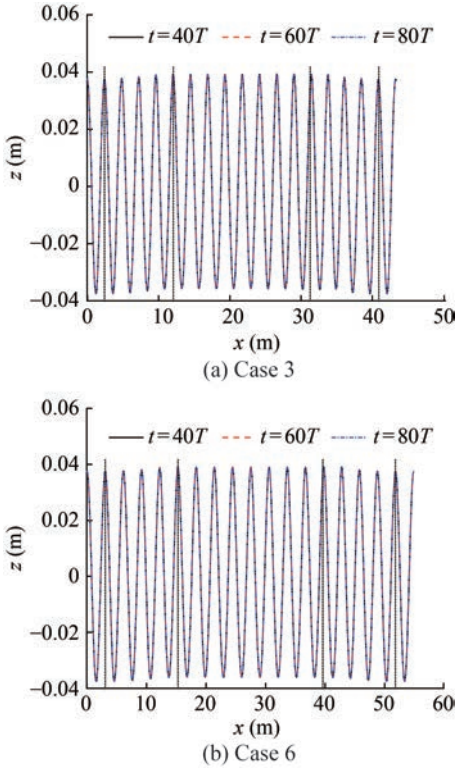

Figure 3 Wave profiles of regular waves in the presence of quadratic shear currents at different times, Cases 3 and 6

Figure 3 presents the wave profiles of regular waves in the presence of quadratic shear currents at $t = 40T$, $60T$, and $80T$. The dashed black line denotes the boundary of the five regions (Figure 1). The wave profiles of regular waves do not change at different times for the opposing-current case and following-current case, and the quasi-steady-state nonlinear waves can be acquired in the nonlinear region. The HLGN model can stably simulate regular waves in the presence of background shear currents. The results of the HLGN model are obtained from the quasi-steady-state nonlinear waves in the nonlinear region, approximately from $x = 6\lambda$ in Section 3.1.

The results of wave profiles in the presence of three types of currents are illustrated in Figure 4. The wave profiles for regular waves in the presence of uniform, linear shear, and quadratic shear currents are compared. The wave profile in the absence of currents is also considered for comparison. The horizontal position of the first wave peak is recentered to $x = 0$.

Figures 4(a) and 4(b) exhibit the wave profile for opposing and following current cases, respectively. Figure 4(a) shows that opposing background currents diminish the wavelength of regular waves. The wavelength of the quadratic shear current case is the largest, and that of the uniform

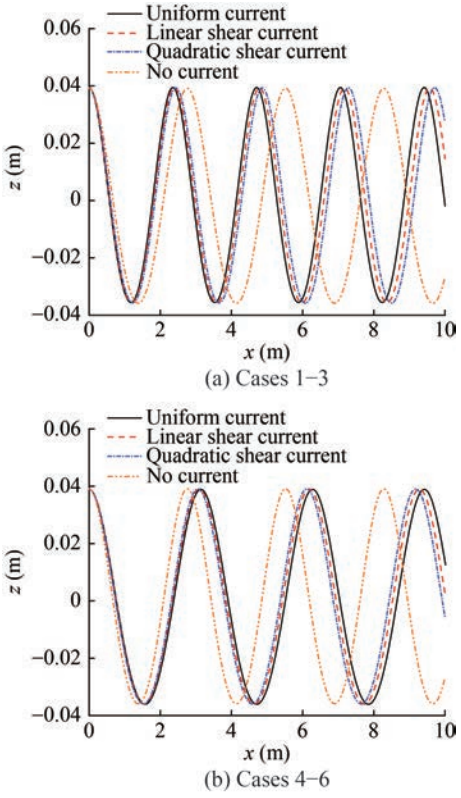

Figure 4 Wave profile of regular waves in the presence of three types of currents with the same velocity at the SWL, Cases 1–6

current is the smallest. Compared with the no-current case, the wavelengths in uniform, linear shear, and quadratic shear currents decrease by 15%, 13%, and 12%, respectively. Figure 4(b) shows that following currents increase the wavelength of regular waves; the smallest wavelength is observed in the quadratic shear current case, and the largest wavelength is in the uniform current case. Compared with the no-current case, the wavelengths in uniform, linear shear, and quadratic shear currents increase by 14%, 12%, and 10%, respectively. Regardless of the current direction, the effect of the uniform current on wavelength is the most pronounced, whereas that of the quadratic shear current is the weakest.

3.1.3 Velocity field

In this subsection, the velocity field of regular waves in background currents is analyzed. The horizontal velocities along the water column under the wave crest of regular waves in uniform, linear shear, and quadratic shear currents are presented in Figure 5, which also shows the results of the no-current case for comparison. Figures 5(a) and 5(b) reveal the results for opposing and following current cases, respectively. Figure 5(a) presents that the opposing current reduces the horizontal velocity. Below the SWL, the horizontal velocities in uniform, linear shear, and quadratic shear currents increase sequentially. Figure 5(b) illustrates that the following current increases the horizontal velocity.

Below the SWL, the horizontal velocities in uniform, linear shear, and quadratic shear currents decrease sequentially. Near the free surface, the horizontal velocities in the three types of background currents are similar.

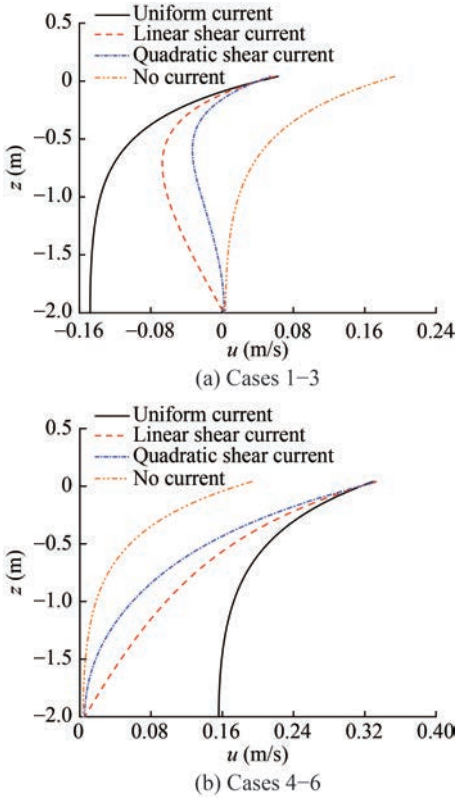

Figure 5 Horizontal velocity along the water column under the wave crest of regular waves in the presence of three types of currents with the same velocity at the SWL, Cases 1–6

Among the three background currents studied in this section, the current velocities of uniform, linear shear, and quadratic shear currents diminish sequentially below the SWL. The flow volume Q of the background current can be determined as follows:

$$Q = \int_{-h}^{0} u_c(z)\,\mathrm{d}z \tag{21}$$

In each case, the current velocity u_c from $-h$ to 0 along the vertical directionz is integrated to acquire the flow volume Q. The flow volume of uniform currents is twice that of linear shear currents and three times that of quadratic shear currents. For the three types of background currents with the same velocity at the SWL, the vertical distribution of the current velocity and the flow volume are considerably different, which leads to variances in the wave profile and velocity field of regular waves.

3.2 Currents with the same flow volume

In this section, the effects of background currents with the same flow volume on regular waves are considered. In the 2D case, the flow volume Q of the background current can be stated as $Q = \tilde{U}h$, where $\tilde{U}$ is the depth-average current velocity. Then, the flow volume of background currents can be denoted by the depth-average current velocity.

3.2.1 Numerical cases

Regular waves in the presence of currents are numerically simulated by the HLGN model. The background currents are described as $u_c = (n+1)\tilde{U}(1+z/h)^n\,(n = 0, 1, 2)$. When n = 0, 1, and 2, the background currents correspond to uniform, linear shear, and quadratic shear currents, respectively. The parameters of the cases are listed in Table 2, and the wave height, period, and water depth are consistent with those in Table 1. The steepness and dispersion of the regular waves without currents are $H/\lambda_0 = 0.0274$ and $h/\lambda_0 = 0.730$, respectively. The computational domain is 20λ long. The lengths of the linear, transition, and nonlinear regions are λ, 5λ, and 8λ, respectively.

Table 2 Parameters of regular waves in background currents with the same flow volume

Case	h(m)	H(m)	T(s)	$\tilde{U}/c_0$	Current type
7	2.0	0.075	1.325	−0.034	Uniform
8	2.0	0.075	1.325	−0.034	Linear shear
9	2.0	0.075	1.325	−0.034	Quadratic shear
10	2.0	0.075	1.325	0.034	Uniform
11	2.0	0.075	1.325	0.034	Linear shear
12	2.0	0.075	1.325	0.034	Quadratic shear

The current velocity profiles of uniform, linear shear, and quadratic shear currents are presented in Figure 6. At the SWL, the current velocity of the quadratic shear current is the strongest, whereas that of the uniform current is the weakest. The velocity of the quadratic shear current is 1.5 times greater than that of the linear shear current and 3 times that of the uniform current. At the bottom, the current velocities of the linear shear current and quadratic shear current are zero. The velocities of uniform, linear shear, and quadratic shear currents increase sequentially at $z > -h/3$. Conversely, at $z < -0.5h$, the current velocities of uniform, linear shear, and quadratic shear currents decrease sequentially.

3.2.2 Wave profile

In this subsection, the wave profile of regular waves is studied. Regular waves in the presence of quadratic shear currents are shown as an example, and the wave profiles at different times are presented in Figure 7.

Figure 7 presents the wave profiles of regular waves in the presence of quadratic shear currents at $t = 70T$, $80T$, and $90T$. The dashed black line denotes the boundary of five regions (Figure 1). The wave profiles of the regular

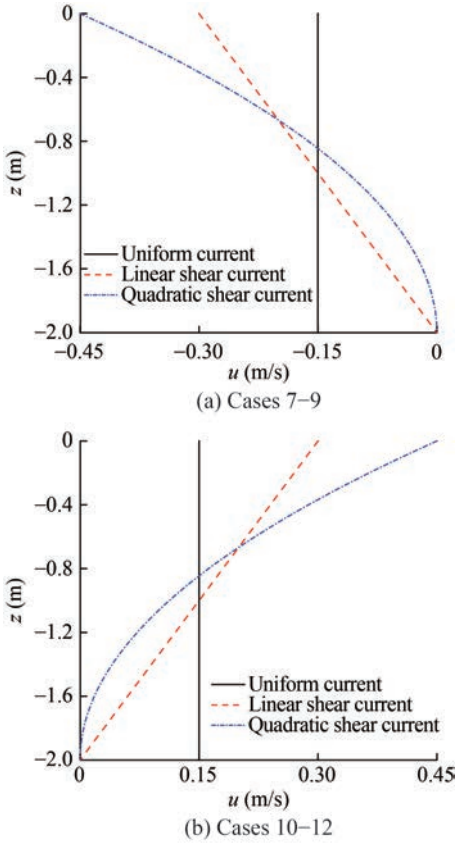

Figure 6 Current velocity profile of three types of background currents, Cases 7–12

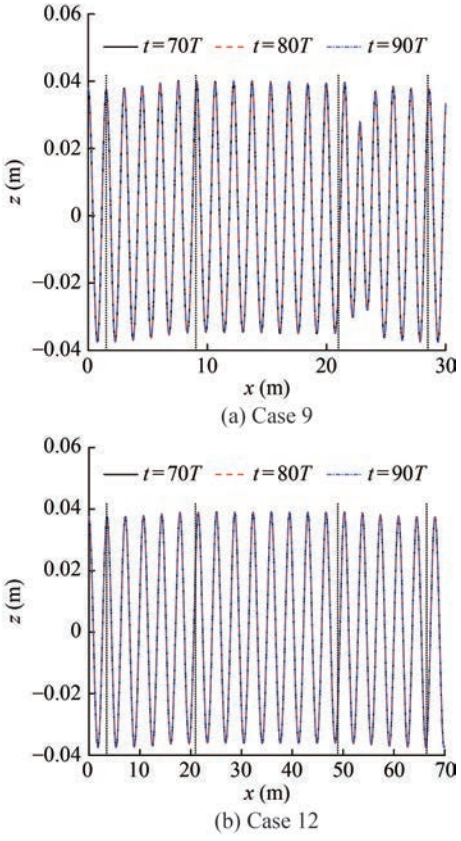

Figure 7 Wave profiles of regular waves in the presence of quadratic shear currents at different times, Cases 9 and 12

waves do not change at different times, and the quasi-steady-state nonlinear waves can be acquired in the nonlinear region. The HLGN results of regular waves in background shear currents are stable. The results of the HLGN model are acquired in the nonlinear region approximately from $x = 7\lambda$ in Section 3.2.

The results of wave profiles in uniform, linear shear, and quadratic shear currents are presented in Figure 8, which also displays the wave profile of the no-current case for comparison. The horizontal position of the first wave peak is recentered to $x = 0$. Figure 8(a) reveals that in the presence of opposing background current, the wavelength of regular waves is substantially reduced, the shortest wavelength occurs in the quadratic shear current cases, and the longest wavelength is in the uniform current case. Compared with the no-current case, the wavelengths in uniform, linear shear, and quadratic shear currents decrease by 14.7%, 28.8%, and 43.7%, respectively. Figure 8(b) presents that following currents increase the wavelength of regular waves, the longest wavelength occurs in the quadratic shear current cases, and the shortest wavelength is in the uniform current case. Compared with the no-current case, the wavelengths in uniform, linear shear, and quadratic shear currents increase by 13.7%, 23.9%, and 30.4%, respectively. Regardless of the direction of the currents, the influence of the uniform current is the weakest, whereas that of the quadratic shear current is the greatest. The opposing current has a greater effect on wavelength compared with the following current.

To study the remarkable differences in wavelength under the three types of background currents with the same flow volume, the vorticity of the background currents without waves is investigated. Because no vertical velocity is in the background current, the vorticity Ω of the background current without waves can be stated as follows:

$$\Omega = -\frac{\partial u_c}{\partial z} \tag{22}$$

Figure 9 exhibits the vertical distribution of vorticity in uniform, linear shear, and quadratic shear currents without waves.

Figure 9 presents that the vorticity of uniform current is zero, the vorticity of linear shear current stays constant with depth, whereas the vorticity of quadratic shear current decreases with depth. At the bottom, the vorticities of uniform and quadratic shear currents are zero, whereas that of the linear shear current is stronger. At $z > -2h/3$, the vorticity of the quadratic shear current is the strongest, and that of the uniform current is the weakest. At the SWL, the vorticity of quadratic shear current is three times greater

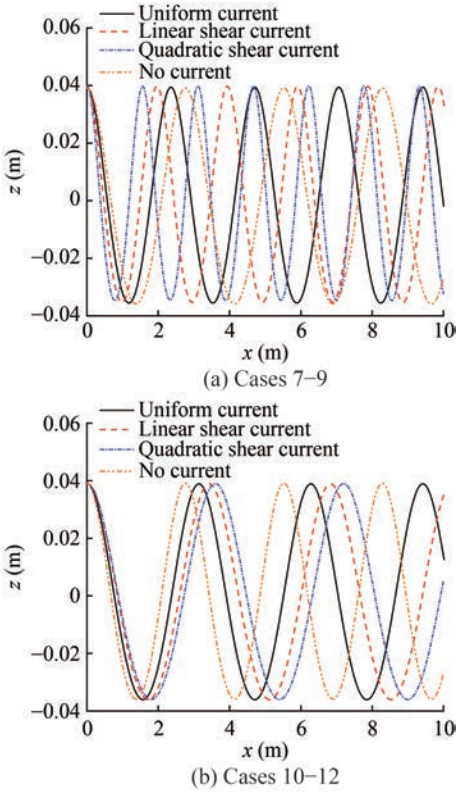

Figure 8 Wave profile of regular waves in the presence of three types of currents with the same flow volume, Cases 7–12

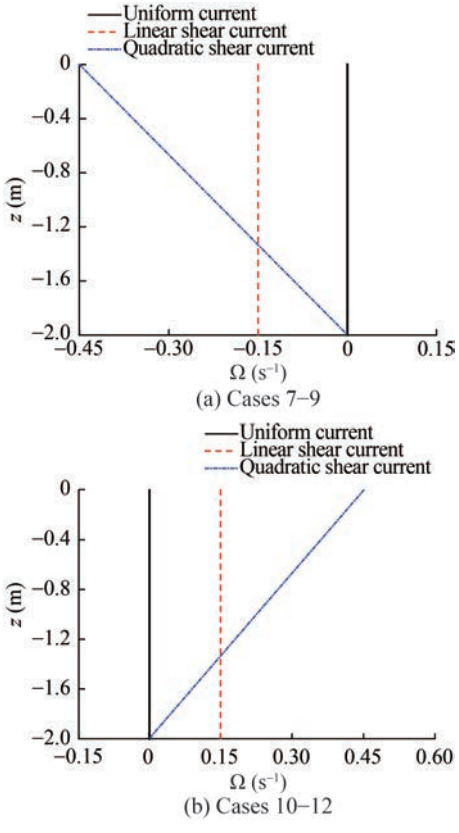

Figure 9 Current vorticity profile of three types of background currents, Cases 7–12

than that of linear shear current. Among the three types of background currents studied in this section, the quadratic shear current with strong velocity and vorticity near the SWL has a more pronounced influence on the wavelength.

3.2.3 Velocity field

In this subsection, the influence of the three types of background currents on the velocity field of regular waves is studied. Figure 10 shows the horizontal velocity along the water column under the wave crest of regular waves in the presence of uniform, linear shear, and quadratic shear currents, which also includes results of the no-current case for comparison.

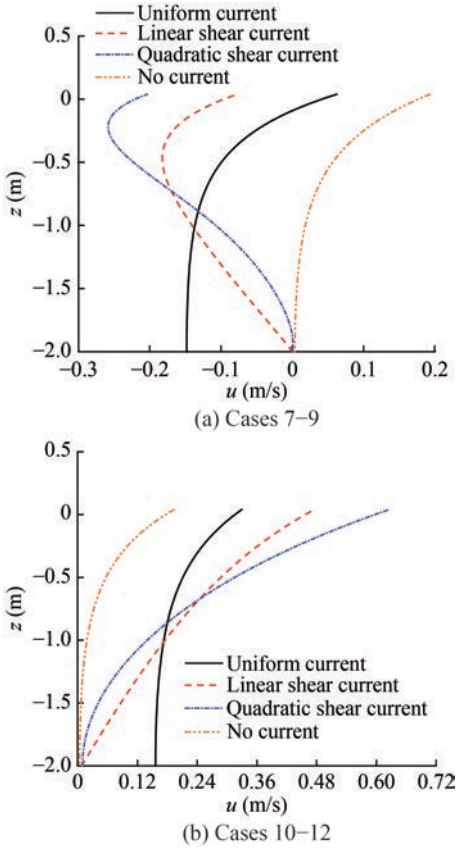

Figure 10 Horizontal velocity along the water column under the wave crest of regular waves in the presence of three types of currents with the same flow volume, Cases 7–12

Figure 10(a) presents that the opposing current reduces the horizontal velocity. Near the bottom (approximately $-1 < z/h < -0.51$), the horizontal velocities in uniform, linear shear, and quadratic shear currents increase sequentially. Near the free surface (approximately $-0.3 < z/h$), the horizontal velocities under the wave crest sequentially decrease in uniform, linear shear, and quadratic shear currents. Figure 10(b) exhibits that the following current increases the horizontal velocity. Near the bottom (approximately $-1 < z/h < -0.51$), the horizontal velocities in uniform, linear shear, and quadratic shear currents decrease

sequentially. Near the free surface (approximately $-0.3 < z/h$), the horizontal velocities under the wave crest sequentially increase in uniform, linear shear, and quadratic shear currents.

$\Delta u_{\max}$ is the difference between the horizontal velocity at the wave crest of regular waves in the background current and that in the no-current case, and $u_{cs} = (n+1)\tilde{U}(n = 0, 1, 2)$ is the background current velocity at the SWL. Under opposing current conditions (Cases 7–9), $\Delta u_{\max}/u_{cs}$ are 0.87, 0.90, and 0.88 for uniform, linear shear, and quadratic shear current cases, respectively. Under following current conditions (Cases 10–12), $\Delta u_{\max}/u_{cs}$ are 0.91, 0.94, and 0.95 for uniform, linear shear, and quadratic shear current cases, respectively.

Combining Figures 10(a) and 10(b) reveals that near the bottom (approximately $-1 < z/h < -0.51$), the influences of uniform, linear shear, and quadratic shear currents on the horizontal velocity along the water column under the wave crest sequentially decrease. Conversely, near the free surface (approximately $-0.3 < z/h$), the effects of uniform, linear shear, and quadratic shear currents sequentially increase. Combining Figures 9 and 10, it is observed that the effects of uniform, linear shear, and quadratic shear currents on the horizontal velocity along the water column under the wave crest are directly linked to the strength of background currents. A stronger current velocity has a more remarkable influence on the horizontal velocity.

3.3 Load of the small-scale vertical cylinder

In this section, the loads on small-scale vertical cylinders subjected to regular waves and three types of background currents with the same flow volume are studied by using the Morison equation.

3.3.1 Morison equation

In engineering design, when $D/\lambda < 0.2$ (where D is the characteristic length of the structure, taken as the cylinder diameter in this paper), the structure is classified as a small-scale structure (DNV, 2021). For the small-scale structure, the total wave force can usually be computed using the Morison equation. The sketch of loads on the small-scale upright cylinder in the wave–current environment is presented in Figure 11.

In the Morison equation, horizontal wave force F_H is represented as the sum of two components: drag force F_D caused by the undisturbed wave field and inertial force F_I resulting from the acceleration field. The F_D and F_I of the unit length of the vertical cylinder are expressed as follows:

$$F_D = \frac{1}{2} C_D \rho D u |u| \tag{23}$$

$$F_I = C_M \rho \frac{\pi D^2}{4} \frac{\partial u}{\partial t} \tag{24}$$

where C_D is the drag coefficient, C_M is the inertial coefficient, and D is the cylinder diameter. In this paper, C_D is 1.2, C_M is 2.0, and ρ is 1 000 kg/m³. When determining the load on the cylinder using the Morison equation, the cylinder is first divided into some small elements. After computing the drag and inertial forces for each element, the overall load on the cylinder is derived by summation. For the cylinder presented in Figure 11, F_H is given by the following equation:

$$F_H = \int_{-h}^{\eta} \frac{1}{2} C_D \rho D u |u| \mathrm{d}z + \int_{-h}^{\eta} C_M \rho \frac{\pi D^2}{4} \frac{\partial u}{\partial t} \mathrm{d}z \tag{25}$$

The height of the cylinder studied in this paper is greater than $h + \eta$; thus, the lower limit of integration is $-h$, and the upper limit is η in Eq. (25). To determine the loads on the cylinder in the wave–current field using Eq. (25), the velocity field of the wave–current environment needs to be obtained. According to the guidelines of DNVGL (DNV, 2021), the velocity field of regular waves in the background current can be estimated by the superposition of the velocity field of regular waves without currents and the background current velocity. In this section, stream function wave theory is employed to determine the velocity field of regular waves without currents. The equation of the background current velocity ignores the effects of the wave surface η. According to the guidelines of DNVGL (DNV, 2021), the Wheeler stretching method can be used to explain the changes in the background current velocity owing to variations in the free surface. The core idea is to introduce a vertical stretching coordinate as follows:

$$z_s = \frac{z - \eta}{h + \eta} h, \quad -h \leqslant z \leqslant \eta, \quad -h \leqslant z_s \leqslant 0 \tag{26}$$

This stretching coordinate transforms the background current velocity of $-h \leqslant z \leqslant \eta$ into $-h \leqslant z_s \leqslant 0$ for calculation, as presented in Figure 12. After stretching the coordinates, the current velocity at the wave surface corresponds to the current velocity on the SWL before stretching.

The linear shear current $u_c(z) = U_0 + U_1 z$ is taken as an example. After introducing the vertical stretching coordinate, the current velocity u_c is expressed as follows:

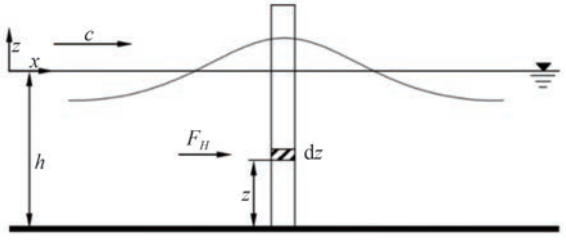

Figure 11 Sketch of the load on the small-scale upright cylinder

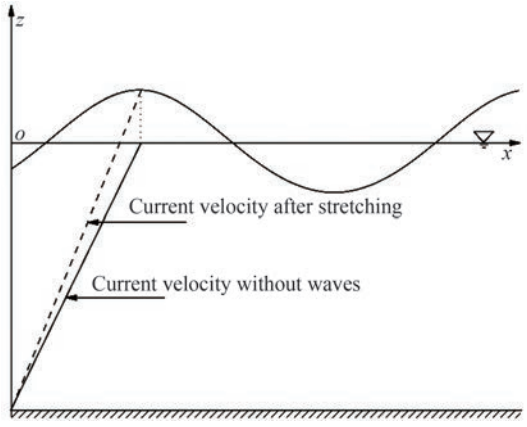

Figure 12 Sketch of stretching the current velocity

$$u_c(z) = U_0 + U_1 z_s = U_0 + \frac{z-\eta}{h+\eta} h U_1 \qquad (27)$$

In this paper, the superposition of the no-current velocity field and the stretched current velocity is referred to as the "stretched superposition method". The parameters for waves and currents are presented in Table 2. The diameter of the vertical cylinder is 0.05 m.

3.3.2 Numerical results

In this subsection, the loads on the small-scale vertical cylinder in regular waves in uniform, linear shear, and quadratic shear currents are computed with the same flow volume based on the velocity field of the HLGN model and the stretched superposition method.

The results of the loads on the small-scale vertical cylinder in regular waves and uniform currents are presented in Figure 13, and the moment of interaction between the wave crest and the small-scale vertical cylinder is recentered to $t = 0$ for comparison.

Figure 13 shows a trough and a peak in the load on the small-scale vertical cylinder over one period. First, the load results based on the velocity field of the HLGN model are studied. Figure 13(a) presents that the load intensity $|F_H|$ of the trough, which represents the maximum load intensity on the cylinder, exceeds that of the peak in the opposing-current case. Conversely, Figure 13(b) reveals that the load intensity $|F_H|$ of the peak, which represents the maximum load intensity on the cylinder, exceeds that of the trough in the following-current case. The maximum load intensity in the opposing current (i.e., the trough load intensity in the opposing current) is lower than that in the following current (i.e., the peak load intensity in the following current).

Then, the load results based on the velocity field of the stretched superposition method are compared with that of the HLGN model to examine the errors of the stretched superposition method in the maximum load intensity (i.e., trough load intensity in opposing currents and peak load intensity in following currents) and load fluctuation amplitude. The stretched superposition method overestimates the maximum load intensity and the load fluctuation amplitude by about 4.7% and about 8.6% in the opposing-current case, respectively, as presented in Figure 13(a), whereas it underestimates the maximum load intensity and the load fluctuation amplitude by about 3.1% and about 6.0% in the following-current cases, respectively, as presented in Figure 13(b).

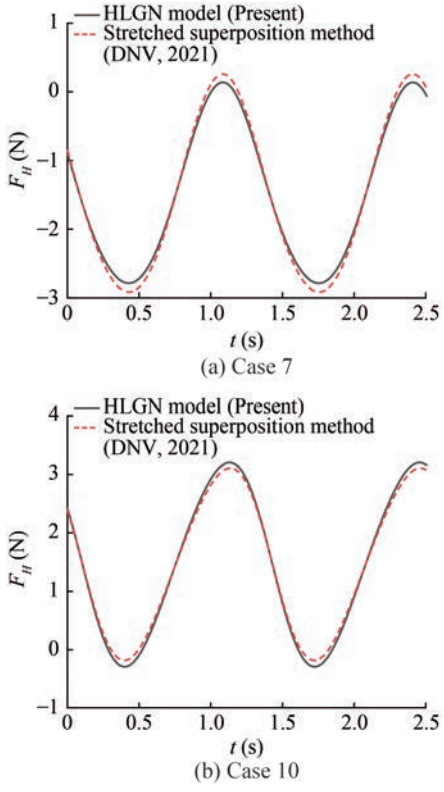

Figure 13 Load of a small-scale upright cylinder in regular waves and uniform currents, Cases 7 and 10

The results of the loads on the small-scale vertical cylinder in regular waves and linear currents are presented in Figure 14, and the moment of interaction between the wave crest and the small-scale vertical cylinder is recentered to $t = 0$ for comparison.

Trough load intensity $|F_H|$ denotes the maximum load intensity that is greater than that of the peak, as presented in Figure 14(a) for the opposing-current case. By contrast, peak load intensity $|F_H|$ signifies the maximum load intensity that is greater than that of the trough, as illustrated in Figure 14(b) for the following-current case. The maximum load intensity in the opposing current is lower than that in the following current. The stretched superposition method overestimates the maximum load intensity and the load fluctuation amplitude by about 8.2% and about 17.1% in the opposing-current case, respectively, as revealed in Figure 14(a), whereas it underestimates the maximum load intensity and the load fluctuation amplitude by about 4.0%

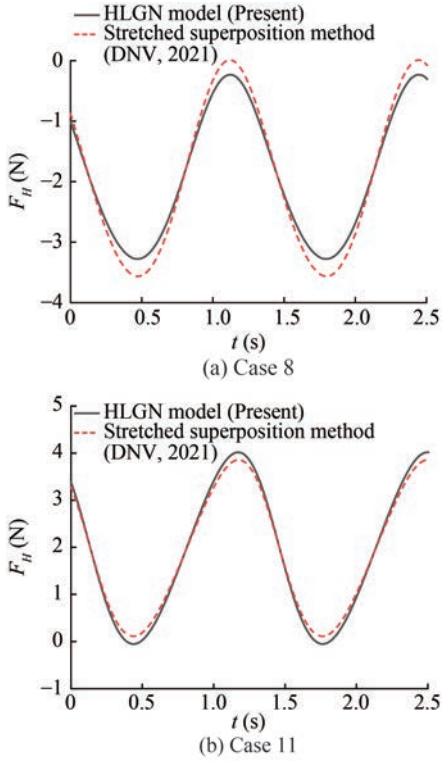

Figure 14 Load of a small-scale upright cylinder in regular waves and linear shear currents, Cases 8 and 11

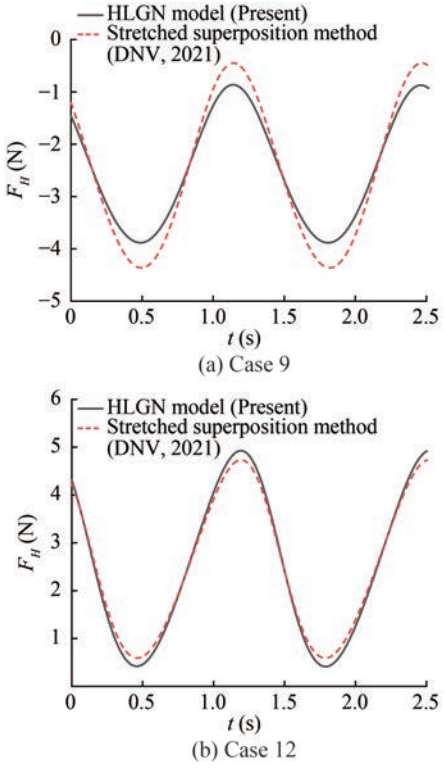

Figure 15 Load of a small-scale upright cylinder in regular waves and quadratic shear currents, Cases 9 and 12

and about 8.0% in the following-current case, respectively, as presented in Figure 14(b).

The results of the loads on the small-scale vertical cylinder in regular waves and quadratic currents are demonstrated in Figure 15, and the moment of interaction between the wave crest and the small-scale vertical cylinder is recentered to $t = 0$ for comparison.

Similar to the uniform and linear shear current cases, the trough load intensity $|F_H|$ exceeds that of the peak, as presented in Figure 14(a) for the opposing-current case, whereas the peak load intensity exceeds that of the trough, as revealed in Figure 14(b) for the following-current case. In addition, the maximum load intensity in the opposing current (i.e., the trough load intensity in the opposing current) is lower than that in the following current (i.e., the peak load intensity in the following current). The stretched superposition method overestimates the maximum load intensity and the load fluctuation amplitude by about 11.8% and about 28.4% in the opposing-current case, respectively, as presented in Figure 14(a), whereas it underestimates the maximum load intensity and the load fluctuation amplitude by about 4.2% and about 9.0% in the following-current case, respectively, as revealed in Figure 14(b).

Figures 13, 14, and 15 present that the maximum load intensity and load fluctuation amplitude in uniform, linear shear, and quadratic shear currents sequentially increase. For the same type of background current, the errors of the stretched superposition method are greater in the opposing-current cases than in the following-current cases. The stretched superposition method overestimates the maximum load intensity and load fluctuation amplitude in opposing-current cases, whereas it underestimates these values in following-current cases. In the following-current case, the load calculation errors of the stretched superposition method are similar in the three types of background currents. However, in the opposing-current cases, the load calculation errors of the stretched superposition method are substantially different among the three types of background currents; the largest errors occur in the quadratic shear current, and the smallest errors occur in the uniform current. This outcome is primarily because the wave nonlinearity in opposing currents is stronger than that in following currents, and the stretched superposition method is less effective in estimating the velocity field for strongly nonlinear waves, which leads to larger errors. In the opposing-current cases, the nonlinearity of the quadratic shear current case is the strongest and thereby results in the largest errors.

4 Conclusions

In this paper, the HLGN model is employed to simulate regular waves in the presence of background currents. Three types of background currents are considered: uni-

form, linear shear, and quadratic shear. The results reveal that the HLGN model can stably simulate regular waves in the presence of the three types of currents.

The wave surface and velocity field of regular waves in the presence of uniform, linear shear, and quadratic shear currents are investigated. In the cases of three background currents with the same velocity at the SWL, owing to the differences in the vertical distribution of background current velocities, remarkable distinctions in the flow volume result in the distinct characteristics of the regular waves. The cases of the three background currents with the same flow volume present that the quadratic shear current with the strong velocity and vorticity near the SWL has a more pronounced effect on the wavelength. A stronger current velocity leads to a more substantial influence on the horizontal velocity.

Subsequently, the loads on small-scale vertical cylinders subjected to regular waves and three types of background currents with the same flow volume are analyzed. The results reveal that the maximum load intensity and load fluctuation amplitude in uniform, linear shear, and quadratic shear currents increase sequentially. The velocity field computed by the stretched superposition method overestimates the maximum load intensity and load fluctuation amplitude in opposing currents but underestimates these values in following currents. The stretched superposition method poorly approximates the velocity field for strongly nonlinear waves and leads to larger load calculation errors. Specifically, in the opposing quadratic shear current, the maximum load intensity calculation error and the load fluctuation amplitude calculation error may reach 11.8% and 28.4%, respectively.

Funding Supported by the Development and Application Project of Ship CAE Software.

Competing interest Wengyang Duan is one of Editors for the Journal of Marine Science and Application and was not involved in the editorial review, or the decision to publish this article. Binbin Zhao is an editorial board member for the Journal of Marine Science and Application and were not involved in the editorial review, or the decision to publish this article. All authors declare that there are no other competing interests.

References

Abbasnia A, Guedes Soares C (2018) Fully nonlinear propagation of waves in a uniform current using NURBS numerical wave tank. Ocean Engineering 163: 115-125. DOI: 10.1016/j.oceaneng.2018.05.039

Baddour RE, Song SW (1998) The rotational flow of finite amplitude periodic water waves on shear currents. Applied Ocean Research 20: 163-171. DOI: 10.1016/S0141-1187(98)00015-7

Banihashemi S, Kirby JT, Dong Z (2017) Approximation of wave action flux velocity in strongly sheared mean flows. Ocean Modelling 116: 33-47. DOI: 10.1016/j.ocemod.2017.06.002

Chen HF, Zou QP (2019) Effects of following and opposing vertical current shear on nonlinear wave interactions. Applied Ocean Research 89: 23-35. DOI: 10.1016/j.apor.2019.04.001

Chen L, Basu B (2021) Numerical continuation method for large-amplitude steady water waves on depth-varying currents in flows with fixed mean water depth. Applied Ocean Research 111: 102631. DOI: 10.1016/j.apor.2021.102631

Chen LF, Ning DZ, Teng B, Zhao M (2017) Numerical and experimental investigation of nonlinear wave-current propagation over a submerged breakwater. Journal of Engineering Mechanics 143(9): 04017061. DOI: 10.1061/(ASCE)EM.1943-7889.0001271

Choi W (2009) Nonlinear surface waves interacting with a linear shear current. Mathematics and Computers in Simulation 80(1): 29-36. DOI: 10.1016/j.matcom.2009.06.021

Constantin A, Escher J (2004) Symmetry of steady periodic surface water waves with vorticity. Journal of Fluid Mechanics 498: 171-181. DOI: 10.1017/S0022112003006773

Constantin A, Kalimeris K, Scherzer O (2015) Approximations of steady periodic water waves in flows with constant vorticity. Nonlinear Analysis-Real World Applications 25: 276-306. DOI: 10.1016/j.nonrwa.2015.04.003

Dalrymple RA (1974) A finite amplitude wave on a linear shear current. Journal of Geophysical Research 79(30): 4498-4504. DOI: 10.1029/JC079i030p04498

Dalrymple RA, Cox JC (1976) Symmetric finite-amplitude rotational water waves. Journal of Physical Oceanography 6(6): 847-852. DOI: 10.1175/1520-0485(1976)006<0847:SFARWW>2.0.CO;2

DNV (2021) DNVGL-RP-C205: Environmental conditions and environmental loads. Det Norske Veritas, Oslo

Duan WY, Zheng K, Zhao BB, Demirbilek Z, Ertekin RC, Webster WC (2016) On wave-current interaction by the Green-Naghdi equations in shallow water. Natural Hazards 84: S567-S583. DOI: 10.1007/s11069-016-2464-0

Hsu HC, Chen YY, Hsu JRC, Tseng WJ (2009) Nonlinear water waves on uniform current in Lagrangian coordinates. Journal of Nonlinear Mathematical Physics 16(1): 47-61. DOI: 10.1142/S1402925109000054

Kirby JT, Chen TM (1989) Surface waves on vertically sheared flows: approximate dispersion relations. Journal of Geophysical Research: Oceans 94: 1013-1027. DOI: 10.1029/JC094iC01p01013

Ko J, Strauss W (2008) Effect of vorticity on steady water waves. Journal of Fluid Mechanics 608: 197-215. DOI: 10.1017/S0022112008002371

Kumar A, Hayatdavoodi M (2023a) On wave-current interaction in deep and finite water depths. Journal of Ocean Engineering and Marine Energy 9: 455-475. DOI: 10.1007/s40722-023-00278-x

Kumar A, Hayatdavoodi M (2023b) Effect of currents on nonlinear waves in shallow water. Coastal Engineering 181: 104278. DOI:

10.1016/j.coastaleng.2023.104278
Li Y, Ellingsen SÅ (2019) A framework for modeling linear surface waves on shear currents in slowly varying waters. Journal of Geophysical Research-Oceans 124(4): 2527-2545. DOI: 10.1029/2018JC014390
Nwogu OG (2009) Interaction of finite-amplitude waves with vertically sheared current fields. Journal of Fluid Mechanics 627: 179-213. DOI: 10.1017/S0022112009005850
Son S, Lynett PJ (2014) Interaction of dispersive water waves with weakly sheared currents of arbitrary profile. Coastal Engineering 90: 64-84. DOI: 10.1016/j.coastaleng.2014.04.009
Steer JN, Borthwick AGL, Stagonas D, Buldakov E, van den Bremer TS (2020) Experimental study of dispersion and modulational instability of surface gravity waves on constant vorticity currents. Journal of Fluid Mechanics 884: A40. DOI: 10.1017/jfm.2019.951
Swan C (1990) An experimental study of waves on a strongly sheared current profile. Proceeding of 22nd Coastal Engineering, Delft, 489-502. DOI: 10.1061/9780872627765.040
Swan C, Cummins IP, James RL (2001) An experimental study of two-dimensional surface water waves propagating on depth-varying currents. Part 1. Regular waves. Journal of Fluid Mechanics 428: 273-304. DOI: 10.1017/S0022112000002457
Swan C, James RL (2000) A simple analytical model for surface water waves on a depth-varying current. Applied Ocean Research 22: 331-347. DOI: 10.1016/S0141-1187(00)00022-5
Thomas GP (1981) Wave-current interactions: an experimental and numerical study. Part 1. Linear waves. Journal of Fluid Mechanics 110: 457-474. DOI: 10.1017/S0022112081000839
Thomas GP (1990) Wave-current interactions: an experimental and numerical study. Part 2. Nonlinear waves. Journal of Fluid Mechanics 216, 505-536. DOI: 10.1017/S0022112090000519
Touboul J, Charland J, Rey V, Belibassakis K (2016) Extended mild-slope equation for surface waves interacting with a vertically sheared current. Coastal Engineering 116: 77-88. DOI: 10.1016/j.coastaleng.2016.06.003
Umeyama M (2011) Coupled PIV and PTV measurements of particle velocities and trajectories for surface waves following a steady current. Journal of Waterway Port Coastal and Ocean Engineering 137(2): 85-94. DOI: 10.1061/(ASCE)WW.1943-5460.0000067
Umeyama M (2017) Dynamic-pressure distributions under Stokes waves with and without a current. Philosophical Transactions of the Royal Society A-Mathematical Physical and Engineering Sciences 376(2111): 20170103.
Yang ZT, Liu PLF (2020) Depth-integrated wave-current models. Part 1. Two-dimensional formulation and applications. Journal of Fluid Mechanics 883: A4. DOI: 10.1017/jfm.2019.831
Yang ZT, Liu PLF (2022) Depth-integrated wave-current models. Part 2. Current with an arbitrary profile. Journal of Fluid Mechanics 936: A31. DOI: 10.1017/jfm.2022.42
Zhang JS, Zhang Y, Jeng DS, Liu PLF, Zhang C (2014) Numerical simulation of wave-current interaction using a RANS solver. Ocean Engineering 75: 157-164. DOI: 10.1016/j.oceaneng.2013.10.014
Zhao BB, Duan WY, Ertekin RC (2014) Application of higher-level GN theory to some wave transformation problems. Coastal Engineering 83: 177-189. DOI: 10.1016/j.coastaleng.2013.10.010
Zhao BB, Li MJ, Duan WY, Ertekin RC, Hayatdavoodi M (2023) An effective method for nonlinear wave-current generation and absorption. Coastal Engineering 185: 104359. DOI: 10.1016/j.coastaleng.2023.104359